

JGR Solid Earth

RESEARCH ARTICLE

10.1029/2018JB017020

Key Points:

- A theoretical framework for calculating 3-D individual and event kernels for multicomponent ambient noise adjoint tomography is developed
- The kernels are validated in a 3-D heterogeneous isotropic medium and can be efficiently computed for adjoint tomographic application
- The method can be extended to construct kernels for radially anisotropic model parameters and Rayleigh wave ellipticity

Supporting Information:

- Supporting Information S1

Correspondence to:

Y. Yang
yingjie.yang@mq.edu.au

Citation:

Wang, K., Liu, Q., & Yang, Y. (2019). Three-dimensional sensitivity kernels for multicomponent empirical Green's functions from ambient noise: Methodology and application to adjoint tomography. *Journal of Geophysical Research: Solid Earth*, 124. <https://doi.org/10.1029/2018JB017020>

Received 15 NOV 2018

Accepted 23 MAY 2019

Accepted article online 29 MAY 2019

Three-Dimensional Sensitivity Kernels for Multicomponent Empirical Green's Functions From Ambient Noise: Methodology and Application to Adjoint Tomography

Kai, Wang^{1,2}, Qinya Liu^{2,3}, and Yingjie, Yang¹

¹ARC Centre of Excellence for Core to Crust Fluid System and GEMOC ARC National Key Centre, Earth and Planetary Sciences, Macquarie University, Sydney, Australia, ²Department of Physics, University of Toronto, Toronto, Canada, ³Department of Earth Sciences, University of Toronto, Toronto, Canada

Abstract Adjoint tomography has recently been applied to ambient noise data as a new and promising tomographic method that utilizes simulation-based 3-D sensitivity kernels rather than ray theory used in traditional ambient noise tomography. However, to date, most studies of ambient noise adjoint tomography only use vertical-component Rayleigh waves. In this study, we develop a theoretical framework for calculating sensitivity kernels for multicomponent empirical Green's functions extracted from ambient noise data. Under the framework of the adjoint method, we demonstrate that a horizontal component (transverse-transverse or radial-radial) kernel can be constructed from the interaction of wave fields generated by point-force sources acting in the north and east directions based on rotation relationships. Our method is benchmarked for a 3-D heterogeneous isotropic model by comparing rotated seismograms, individual, and event traveltimes misfit kernels with corresponding references computed by numerical simulations with sources directly placed in the radial or transverse directions. Based on our new method, we perform the first Love-wave ambient noise adjoint tomography in southern California and construct an improved V_{SH} model. Our method for computing sensitivity kernels of multicomponent empirical Green's functions provides the basis for multicomponent ambient noise adjoint tomography in imaging radially anisotropic shear-wave velocity structures.

1. Introduction

In the past few years, surface waves from ambient noise cross-correlation functions (NCFs) have been used in full-wave inversions through either the scattering-integral (e.g., Zhao et al., 2005) or adjoint method (e.g., Tromp et al., 2005) based on numerical methods for seismic wave simulations such as finite-difference modeling (e.g., Gao & Shen, 2014; Lee et al., 2014) or spectral element method (SEM; e.g., Chen et al., 2014; Wang et al., 2018; Zhu, 2018). Compared with conventional ambient noise tomography (ANT; e.g., Bensen et al., 2007; Lin et al., 2007; Sabra et al., 2005; Shapiro et al., 2005; Yang et al., 2007; Yao et al., 2006), such simulation-based ANT differs in several aspects: (1) Phase traveltimes misfits in multiple period bands (e.g., Chen et al., 2014; Wang et al., 2018; Zhu, 2018) are measured instead of dispersion curves (e.g., Bensen et al., 2007; Shapiro et al., 2005); (2) iterative optimization inversion (e.g., Luo, 2012; Tape et al., 2009; Zhu et al., 2012) is used to directly invert for Vs structures instead of the intermediate step of constructing period-dependent 2-D phase maps (e.g., Lin et al., 2008; Yang et al., 2007; Yao et al., 2006) followed by a 1-D inversion for depth-dependent Vs structure (e.g., Bensen et al., 2009; Luo et al., 2015; Yao et al., 2008) (two-step inversion); and (3) accurate 3-D kernels are computed based on numerical methods (Liu & Tromp, 2006; Zhao et al., 2005) instead of ray theory (e.g., Barmin et al., 2001; Rawlinson & Sambridge, 2004) and other analytic methods (Herrmann & Ammon, 2004; Masters et al., 2007) used in the two-step inversion. The simulation-based method has shown several advantages over traditional ANT, including more realistic sensitivity kernels for 3-D structural updates and more resolving power for strong velocity variations (e.g., Chen et al., 2014; Wang et al., 2018).

Currently, ambient noise adjoint tomography (ANAT) or simulation-based ANT studies have only utilized vertical-vertical (Z-Z) component Rayleigh-wave empirical Green's functions (EGFs) extracted from

vertical-component ambient noise to resolve isotropic structures. No ANAT study has attempted to use signals from other components, such as Love-wave signals from transverse-transverse (T-T) component, presumably owing to significant computational cost needed to construct T-T or radial-radial (R-R) component kernels based on numerical simulations. Additional T-T and R-R component EGFs in ANAT are complementary to Z-Z component EGFs and allow the inversion for vertical-polarized (V_{SV}) and horizontal-polarized (V_{SH}) shear-wave velocities, that is, radial anisotropy. This calls for an efficient computation method of constructing *event kernels* (Tape et al., 2007) for horizontal-component (T-T and R-R) EGFs in ANAT, which is the primary goal of this study.

To compute the event kernels for Rayleigh-wave type ANAT using only Z-Z component EGFs, a vertical point-force source is first implemented at the master station on the surface to generate the forward wavefield. Then the adjoint wavefield is constructed by placing vertical adjoint sources at all receivers and is time convolved with the forward wavefield to generate the event kernel. The reason that adjoint sources can be applied simultaneously at all receivers is because all these sources act in the vertical direction. In comparison, for Love-wave type ANAT, a transverse-component point-force source needs to be injected at the master station for the forward field as well as at each receiver for the adjoint field. However, since different source-receiver pairs have different azimuths, it becomes impossible to construct a similar event kernel for all receivers with only one forward and adjoint simulation. In order to solve this problem, we propose to perform two forward simulations (with a point force injected in the north or east direction at the master station) and two adjoint simulations. The resulting two kernels from time convolution of these forward and adjoint fields can be summed to obtain a T-T or R-R kernel based on rotation relationships.

This paper is organized as follows: In section 2, we derive the formulas for computing multicomponent individual and event kernels based upon rotation relationships. Then in section 3, the rotated seismograms and kernels are validated by numerical simulations. To demonstrate the applicability of these event kernels, in section 4, we apply our method to imaging V_{SH} structures beneath southern California based on T-T component Love-wave EGFs. Finally, in section 5, we extend the concept of our method to the construction of 3-D kernels for radially anisotropic velocity parameters and Rayleigh-wave ellipticity and also briefly discuss the effect of unevenly distributed noise sources on the construction of 3-D kernels.

2. Methodology

The theory of adjoint tomography (sometimes is also referred to as full-wave inversions) has been well documented in the literature (e.g., Fichtner, 2010; Liu & Gu, 2012; Tromp et al., 2005). Based on the formal kernel expressions in Tromp et al. (2005), we introduce a compact expression for a generic kernel as

$$K(\mathbf{x}) = \mathbf{u}(\mathbf{x}, t; \mathbf{x}_s) \otimes \mathbf{u}^\dagger(\mathbf{x}, T - t; \mathbf{x}_r), \quad (1)$$

where $\mathbf{u}(\mathbf{x}, t; \mathbf{x}_s)$ is a forward wavefield emitted from a source \mathbf{x}_s and $\mathbf{u}^\dagger(\mathbf{x}, T - t; \mathbf{x}_r)$ is an adjoint wavefield generated by the time-reversed adjoint sources injected at receivers \mathbf{x}_r . The \otimes operator represents different interactions of the forward and adjoint field for different types of kernels; the detailed expressions can be found in Appendix A. Note that here the background model through which both forward and adjoint wavefields propagate can be either isotropic or anisotropic.

2.1. Rotation of Coordinate Systems

As rotations of seismograms are involved in constructing multicomponent adjoint sources, we define an orthonormal matrix A that represents the rotation from a *natural* coordinate system with unit vectors in the east, north, and vertical directions, $\{\hat{\mathbf{x}}_j\} = (\hat{\mathbf{x}}_e, \hat{\mathbf{x}}_n, \hat{\mathbf{x}}_v)$ to a *general* coordinate system (e.g., with unit vectors in the transverse, radial, and vertical directions, $\{\hat{\mathbf{x}}^I\} = (\hat{\mathbf{x}}^T, \hat{\mathbf{x}}^R, \hat{\mathbf{x}}^Z)$), such that

$$\hat{\mathbf{x}}^I(\theta) = \sum_j A_j^I(\theta) \hat{\mathbf{x}}_j, \quad \text{and} \quad A_j^I(\theta) = \begin{bmatrix} \cos \theta & -\sin \theta & 0 \\ \sin \theta & \cos \theta & 0 \\ 0 & 0 & 1 \end{bmatrix}, \quad (2)$$

where I and j represent the row and column index of matrix A and each general component is a weighted sum of the three natural components, such as $\hat{\mathbf{x}}^T(\theta) = \cos \theta \hat{\mathbf{x}}_e - \sin \theta \hat{\mathbf{x}}_n$. θ is the azimuth of the radial vector $\hat{\mathbf{x}}^R$ clockwise from $\hat{\mathbf{x}}_n$, as shown in Figure 1a. For the spherical Earth (Figure 1b), the azimuth of the radial vector at the source (θ) may be different from the azimuth of the radial vector at the receiver (θ'), but for a flat Earth approximation, $\theta = \theta'$. Note that for a fixed source at \mathbf{x}_s , θ and θ' vary as a function of

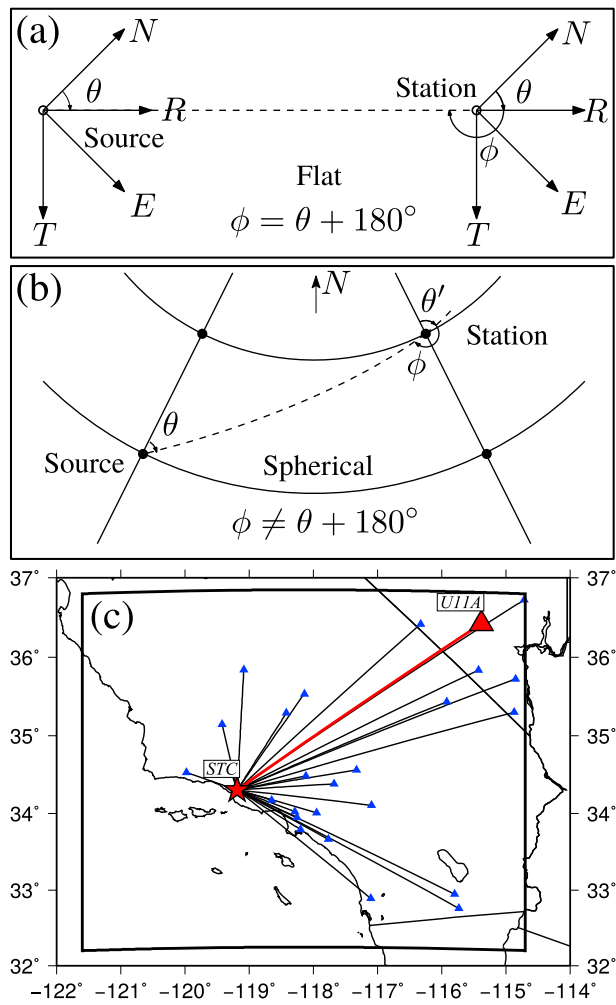


Figure 1. Definition of the azimuth of the radial direction at the source (θ) and the station (θ'), as well as station back-azimuth, $\phi=\theta'+180^\circ$, for a flat (a) and spherical Earth (b). For the flat Earth case, $\theta'=\theta=\phi-180^\circ$. (c) Stations (star and triangles) used for kernel calculations within our simulation region of southern California (outlined by the solid black rectangle). The red star is the master station CLSTC, and the blue triangles are 26 other regional stations with TA.U11A shown in red color. The red solid line connecting CLSTC and TA.U11A indicates the station pair selected for calculating examples of synthetic seismograms and individual kernels in this study, with the azimuth of the radial direction, $\theta=54.68^\circ$ at the source and $\theta'=56.87^\circ$ at the station, and the station back-azimuth $\phi=236.87^\circ$.

the receiver position \mathbf{x}_r , that is, the azimuth angles are generally different for different receivers. Also, the rotation formula can be applied at either the source or the receiver side.

2.2. Forward Wavefield, Adjoint Sources, and Individual Sensitivity Kernels

Let us first consider the sensitivity kernel for a measurement made on a single source-station pair. The source-receiver plane has a surface azimuth of θ (Figure 1a) at the source and surface azimuth of θ' at the receiver. For the master station at \mathbf{x}_s , we define the forward field generated by a Delta-function point force in the $\hat{\mathbf{x}}^I$ direction as $\mathbf{u}^I(\mathbf{x}, t; \mathbf{x}_s)$. It can be related to the forward wavefield generated by a Delta-function point force placed at the source side in the $\hat{\mathbf{x}}_j$ direction, $\mathbf{u}_j(\mathbf{x}, t; \mathbf{x}_s)$, as

$$\mathbf{u}^I(\mathbf{x}, t; \mathbf{x}_s) = \sum_j A_j^I(\theta) \mathbf{u}_j(\mathbf{x}, t; \mathbf{x}_s). \quad (3)$$

According to equation (2), the rotation formula at the receiver side is given by

$$\hat{\mathbf{x}}^J(\theta') = \sum_k A_k^J(\theta') \hat{\mathbf{x}}_k, \quad (4)$$

where J and k are the index in the general and natural coordinate systems, respectively. For an EGF extracted from the NCF between the I th component of the displacement at the master station, and the J th component of the displacement at the receiver station \mathbf{x}_r , referred to as $d^{IJ}(\mathbf{x}_r, t; \mathbf{x}_s)$, its corresponding synthetic Green's function (SGF) can be extracted from the J th component of the forward field $\mathbf{u}^I(\mathbf{x}_r, t; \mathbf{x}_s)$ at the receiver and rewritten as

$$\begin{aligned} \hat{\mathbf{x}}^J(\theta') \cdot \mathbf{u}^I(\mathbf{x}_r, t; \mathbf{x}_s) &= \left[\sum_k A_k^J(\theta') \hat{\mathbf{x}}_k \right] \cdot \left[\sum_j A_j^I(\theta) \mathbf{u}_j(\mathbf{x}_r, t; \mathbf{x}_s) \right] \\ &= \sum_k \sum_j [A_j^I(\theta) A_k^J(\theta')] [\hat{\mathbf{x}}_k \cdot \mathbf{u}_j(\mathbf{x}_r, t; \mathbf{x}_s)]. \end{aligned} \quad (5)$$

In the general coordinate system (section 2.1), as the source force direction $\hat{\mathbf{x}}^I$ (e.g., $I = T$ or R) may vary depending on the azimuth of the receiver θ , the synthetics $\mathbf{u}^I(\mathbf{x}_r, t; \mathbf{x}_s)$ for all receivers cannot be computed in one single forward simulation. However, based on equation (5), the J 'th component of \mathbf{u}^I can be constructed through the weighted sums of $\mathbf{u}_j(\mathbf{x}_r, t; \mathbf{x}_s)$ ($j = e, n, z$), the wavefield generated by a source in the $\hat{\mathbf{x}}_j$ direction, which can be computed for all receivers through one forward simulation (for every j).

For specific I and J directions, we can define an auxiliary matrix \mathbf{C}^{IJ} for a source-receiver pair as

$$C_{jk}^{IJ}(\theta, \theta') = A_j^I(\theta) A_k^J(\theta'), \quad (6)$$

where j and k are the row and column index of \mathbf{C}^{IJ} . Utilizing equation (2), we can obtain the auxiliary matrices for measurements made for Z-Z, T-T, and R-R components as

$$\begin{aligned} \mathbf{C}^{ZZ} &= \begin{bmatrix} 0 & 0 & 0 \\ 0 & 0 & 0 \\ 0 & 0 & 1 \end{bmatrix}, \quad \mathbf{C}^{TT} = \begin{bmatrix} \cos \theta \cos \theta' & -\cos \theta \sin \theta' & 0 \\ -\sin \theta \cos \theta' & \sin \theta \sin \theta' & 0 \\ 0 & 0 & 0 \end{bmatrix}, \\ \mathbf{C}^{RR} &= \begin{bmatrix} \sin \theta \sin \theta' & \sin \theta \cos \theta' & 0 \\ \cos \theta \sin \theta' & \cos \theta \cos \theta' & 0 \\ 0 & 0 & 0 \end{bmatrix}, \end{aligned} \quad (7)$$

and expressions of auxiliary matrice for cross-component SGFs can be found in Appendix B. Thus, the corresponding SGFs for these three types of measurements become

$$\hat{\mathbf{x}}^Z \cdot \mathbf{u}^Z = \hat{\mathbf{x}}_z \cdot \mathbf{u}_z, \quad (8)$$

$$\begin{aligned} \hat{\mathbf{x}}^T \cdot \mathbf{u}^T &= [(\cos \theta \cos \theta') \hat{\mathbf{x}}_e - (\cos \theta \sin \theta') \hat{\mathbf{x}}_n] \cdot \mathbf{u}_e \\ &\quad + [-(\sin \theta \cos \theta') \hat{\mathbf{x}}_e + (\sin \theta \sin \theta') \hat{\mathbf{x}}_n] \cdot \mathbf{u}_n, \end{aligned} \quad (9)$$

$$\begin{aligned} \hat{\mathbf{x}}^R \cdot \mathbf{u}^R &= [(\sin \theta \sin \theta') \hat{\mathbf{x}}_e + (\sin \theta \cos \theta') \hat{\mathbf{x}}_n] \cdot \mathbf{u}_e \\ &\quad + [(\cos \theta \sin \theta') \hat{\mathbf{x}}_e + (\cos \theta \cos \theta') \hat{\mathbf{x}}_n] \cdot \mathbf{u}_n. \end{aligned} \quad (10)$$

Clearly, equation (8) states the fact that the SGFs corresponding to Z-Z component EGFs can be extracted from the vertical component of the forward wavefield generated by a vertical force, in either the natural or general coordinate system. However, according to equations (9) and (10), the horizontal component SGFs are the weighted sum of the forward fields generated by point sources placed in the east and north directions with proper sine/cosine rotation factors as weights.

The EGF, $d^{IJ}(\mathbf{x}_r, t; \mathbf{x}_s)$, and the corresponding SGF, $\hat{\mathbf{x}}^J \cdot \mathbf{u}^I(\mathbf{x}_r, t; \mathbf{x}_s)$, can then be used to construct the associated adjoint source $f^{IJ}(\mathbf{x}_r, t; \mathbf{x}_s)$ (Tromp et al., 2005). This adjoint source time function should be placed in the $\hat{\mathbf{x}}^J$ direction ($J = T, R, Z$) and in practice is injected in all $\hat{\mathbf{x}}_k$ ($k = e, n, z$) directions at the receiver as a source vector:

$$\mathbf{f}^J(\mathbf{x}_r, t; \mathbf{x}_s) = f^{IJ}(\mathbf{x}_r, t; \mathbf{x}_s) \hat{\mathbf{x}}^J = \sum_k [f^{IJ}(\mathbf{x}_r, t; \mathbf{x}_s) A_k^J(\theta')] \hat{\mathbf{x}}_k. \quad (11)$$

The resulting adjoint wavefield, $(\mathbf{u}^\dagger)^J$, is given by

$$\begin{aligned} (\mathbf{u}^\dagger)^J(\mathbf{x}, t; \mathbf{x}_r) &= f^{IJ}(\mathbf{x}_r, t; \mathbf{x}_s) * \mathbf{u}^J(\mathbf{x}, t; \mathbf{x}_r) \\ &= \sum_k [f^{IJ}(\mathbf{x}_r, t; \mathbf{x}_s) A_k^J(\theta')] * \mathbf{u}_k(\mathbf{x}, t; \mathbf{x}_r), \end{aligned} \quad (12)$$

where $\mathbf{u}^J(\mathbf{x}, t; \mathbf{x}_r)$ is the wavefield at \mathbf{x} generated by a Delta-function source in the \mathbf{x}^J direction at \mathbf{x}_r and $*$ represents time convolution.

Substituting equations (3) and (12) to equation (1), the generic expression for the sensitivity kernel of the I - J component EGF measurement at a given source-receiver pair becomes

$$\begin{aligned} K^{IJ}(\mathbf{x}; \mathbf{x}_r, \mathbf{x}_s) &= \mathbf{u}^I(\mathbf{x}, t; \mathbf{x}_s) \otimes (\mathbf{u}^\dagger)^J(\mathbf{x}, T-t; \mathbf{x}_r) \\ &= \sum_j \mathbf{u}_j(\mathbf{x}, t; \mathbf{x}_s) \otimes \sum_k \left\{ [A_j^I(\theta) A_k^J(\theta') f^{IJ}(T-t)] * \mathbf{u}_k(\mathbf{x}, T-t; \mathbf{x}_r) \right\} \\ &= \sum_j \mathbf{u}_j(\mathbf{x}, t; \mathbf{x}_s) \otimes \sum_k \left\{ [C_{jk}^{IJ}(\theta, \theta') f^{IJ}(T-t)] * \mathbf{u}_k(\mathbf{x}, T-t; \mathbf{x}_r) \right\}, \end{aligned} \quad (13)$$

where we drop the $(\mathbf{x}_r, \mathbf{x}_s)$ dependency of the adjoint source f^{IJ} for more compact expressions. Using the auxiliary matrix shown in equation (7), we can write out detailed expressions for sensitivity kernels of different ambient noise measurements.

2.2.1. Z-Z Component Sensitivity Kernels

Let $I = J = Z$ in equation (13), then we have

$$K^{ZZ}(\mathbf{x}; \mathbf{x}_r, \mathbf{x}_s) = \mathbf{u}_z(\mathbf{x}, t; \mathbf{x}_s) \otimes \{f^{ZZ} * \mathbf{u}_z(\mathbf{x}, T-t; \mathbf{x}_r)\}, \quad (14)$$

which suggests that the individual kernel for Z-Z component EGFs can be constructed from the interaction of the forward field from a Delta-function vertical point force at \mathbf{x}_s and the adjoint field due to an adjoint source time function f^{ZZ} injected at the receiver in the vertical direction. Equation (14) shows exactly how sensitivity kernels are computed in Rayleigh-wave type ANAT (e.g., Chen et al., 2014; Wang et al., 2018). The adjoint source f^{ZZ} is constructed from the measurement made between the Z-Z component EGF and the corresponding SGF at the receiver. In the above expressions, the $(\mathbf{x}_r, T-t; \mathbf{x}_s)$ dependence of f^{ZZ} is omitted to reduce symbol clutter.

2.2.2. T-T Component Sensitivity Kernels

Let $I = J = T$ in equation (13), then we have

$$K^{TT}(\mathbf{x}; \mathbf{x}_r, \mathbf{x}_s) = K^{ET}(\mathbf{x}; \mathbf{x}_r, \mathbf{x}_s) + K^{NT}(\mathbf{x}; \mathbf{x}_r, \mathbf{x}_s), \quad (15)$$

where

$$\begin{aligned} K^{ET}(\mathbf{x}; \mathbf{x}_r, \mathbf{x}_s) &= \mathbf{u}_e(\mathbf{x}, t; \mathbf{x}_s) \otimes [(\cos \theta \cos \theta' f^{TT}) * \mathbf{u}_e(\mathbf{x}, T - t; \mathbf{x}_r) \\ &\quad - (\cos \theta \sin \theta' f^{TT}) * \mathbf{u}_n(\mathbf{x}, T - t; \mathbf{x}_r)], \\ K^{NT}(\mathbf{x}; \mathbf{x}_r, \mathbf{x}_s) &= \mathbf{u}_n(\mathbf{x}, t; \mathbf{x}_s) \otimes [-(\sin \theta \cos \theta' f^{TT}) * \mathbf{u}_e(\mathbf{x}, T - t; \mathbf{x}_r) \\ &\quad + (\sin \theta \sin \theta' f^{TT}) * \mathbf{u}_n(\mathbf{x}, T - t; \mathbf{x}_r)]. \end{aligned} \quad (16)$$

This suggests that the sensitivity kernel for measurements on T-T component EGFs can be constructed by the summation of two kernels. The first kernel $K^{ET}(\mathbf{x}; \mathbf{x}_r, \mathbf{x}_s)$ is from the time convolution of a forward field due to a point force in the east direction, $\mathbf{u}_e(\mathbf{x}, t; \mathbf{x}_s)$, and an adjoint field obtained by injecting f^{TT} in the east and north directions at the receiver, with the amplitude modulated by $\cos \theta \cos \theta'$ and $-\cos \theta \sin \theta'$, respectively. The other kernel $K^{NT}(\mathbf{x}; \mathbf{x}_r, \mathbf{x}_s)$ can be constructed in a similar fashion, except that the forward field is now generated by a point-force source in the north direction and the amplitude modulation factors for the adjoint source are $-\sin \theta \cos \theta'$ and $\sin \theta \sin \theta'$, respectively. Therefore, two forward simulations and two adjoint simulations are required to compute the sensitivity kernel for a measurement made on the T-T component EGF for a source-receiver station pair.

2.2.3. R-R Component Sensitivity Kernels

Let $I = J = R$ in equation (13), then we have

$$K^{RR}(\mathbf{x}; \mathbf{x}_r, \mathbf{x}_s) = K^{ER}(\mathbf{x}; \mathbf{x}_r, \mathbf{x}_s) + K^{NR}(\mathbf{x}; \mathbf{x}_r, \mathbf{x}_s), \quad (17)$$

where

$$\begin{aligned} K^{ER}(\mathbf{x}; \mathbf{x}_r, \mathbf{x}_s) &= \mathbf{u}_e(\mathbf{x}, t; \mathbf{x}_s) \otimes [(\sin \theta \sin \theta' f^{RR}) * \mathbf{u}_e(\mathbf{x}, T - t; \mathbf{x}_r) \\ &\quad + (\sin \theta \cos \theta' f^{RR}) * \mathbf{u}_n(\mathbf{x}, T - t; \mathbf{x}_r)], \\ K^{NR}(\mathbf{x}; \mathbf{x}_r, \mathbf{x}_s) &= \mathbf{u}_n(\mathbf{x}, t; \mathbf{x}_s) \otimes [(\cos \theta \sin \theta' f^{RR}) * \mathbf{u}_e(\mathbf{x}, T - t; \mathbf{x}_r) \\ &\quad + (\cos \theta \cos \theta' f^{RR}) * \mathbf{u}_n(\mathbf{x}, T - t; \mathbf{x}_r)]. \end{aligned} \quad (18)$$

Clearly, the sensitivity kernel for R-R component EGFs is also the sum of two kernels, similar to that for the T-T component kernel in equation (16), except that the adjoint source f^{RR} and the amplitude modulation factors are different. In practice, once the T-T component kernel is computed, no more forward simulations are needed, and only two additional adjoint simulations are required for constructing the R-R component kernel.

2.3. Event Kernels for Ambient Noise Measurements

Now we consider an event kernel associated with a selected master station at \mathbf{x}_s and a number of receivers \mathbf{x}_r , $r = 1, \dots, N$. The event kernel is effectively a summation of individual kernels in equation (13) and can be written as

$$\begin{aligned} K^H(\mathbf{x}; \mathbf{x}_s) &= \sum_{r=1}^N \mathbf{u}^I(\mathbf{x}, t; \mathbf{x}_s) \otimes (\mathbf{u}^\dagger)^J(\mathbf{x}, T - t; \mathbf{x}_r) \\ &= \sum_j \mathbf{u}_j(\mathbf{x}, t; \mathbf{x}_s) \otimes \sum_k \sum_{r=1}^N \left\{ \left[C_{jk}^{II}(\theta, \theta') f^H \right] * \mathbf{u}_k(\mathbf{x}, T - t; \mathbf{x}_r) \right\}, \end{aligned} \quad (19)$$

which suggests that computing the event kernel for a selected source station and a number of receivers also requires two forward and two adjoint simulations as in sections 2.2.2 and 2.2.3, except that the modulated adjoint sources for individual receivers are injected simultaneously to compute the combined adjoint wavefield (Tromp et al., 2005). In the following, we refer to the kernels constructed by this method as *rotated* kernels.

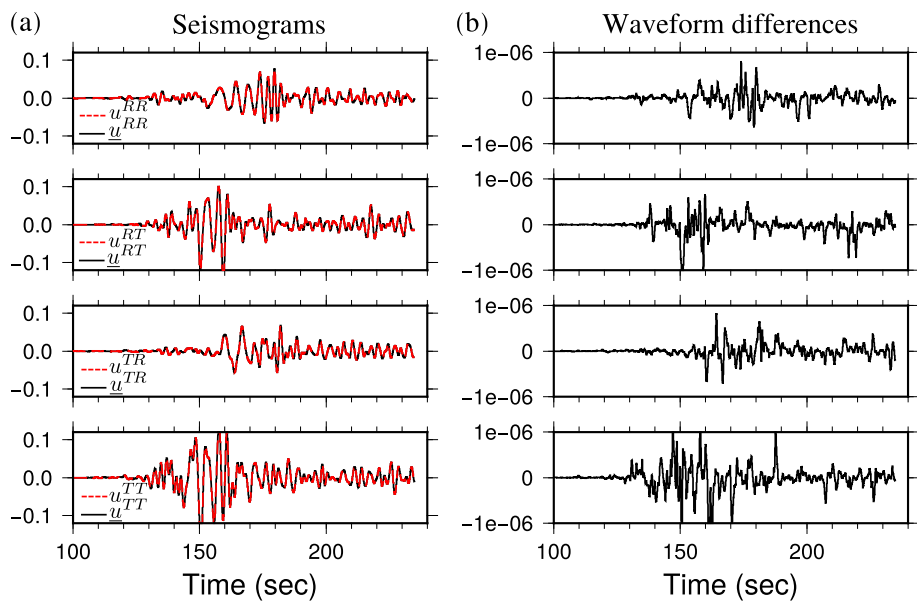


Figure 2. (a) Comparison of the reference and rotated seismograms for the station pair CI.STC-TA.U11A. These seismograms are low-pass filtered with a cutoff period of 2 s, that is, the minimum resolving period of spectral element method. The black solid lines are reference seismograms generated by a radial or a transverse point-force source; the red dashed lines correspond to seismograms calculated from the rotation formulas (9) and (10). (b) Waveform differences between the reference and rotated seismograms in (a). Note the amplitudes of these differences are less than 0.001% of the maximum amplitude of waveforms in (a).

3. Kernel Benchmarks Based on Numerical Simulations

In this section, we conduct three groups of numerical simulations based on a 3-D heterogeneous isotropic model to validate the rotation relationships for seismograms (equation (5)), individual kernels (equations (14)–(18)), and event kernels (equation (19)) derived in section 2. All numerical simulations are conducted using an open-source package SPECFEM3D based on SEM (<https://github.com/geodynamics/specfem3d>) for a 3-D southern California velocity model constructed by Wang et al. (2018) based on Rayleigh wave ANAT. The mesh used for the numerical simulations is the same as that described in Wang et al. (2018) with the accuracy down to a period of 2 s. Throughout this section, we construct multitaper traveltime misfit kernels (Laske & Masters, 1996; Tape et al., 2010; Zhou et al., 2004) between a source (CI.STC) and a number of receivers (Figure 1c) for T-T and R-R component measurements made between EGFs and SGFs. For the purpose of benchmarking, we first perform forward and adjoint simulations by placing point-force sources in the transverse and radial directions to construct the reference SGFs, individual, and event kernels. Then, these SGFs and kernels are utilized to validate the rotated SGF seismograms and kernels, which are actually used for the practical tomographic application.

3.1. Synthetic Green's Functions

For the station pair CI.STC-TA.U11A (Figure 1c), we first compute synthetics for a unidirectional point-force source polarized in the radial, transverse, and east or north direction, separately (Figure S1 in the supporting information). The two east and north component synthetics, u^{RE} and u^{RN} , of the forward wavefield $\underline{\mathbf{u}}^R$ from a source in the radial direction are rotated to obtain the two reference seismograms, \underline{u}^{RR} and \underline{u}^{RT} , where the first upper index indicates the source direction and the second upper index indicates the displacement component recorded at a receiver. Similarly, u^{TE} and u^{TN} of the forward wavefield $\underline{\mathbf{u}}^T$ from a source in the transverse direction are rotated to obtain the two reference seismograms, \underline{u}^{TT} and \underline{u}^{TR} . We also sum up the four north and east component synthetics (u^{EN} , u^{EE} , u^{NE} , and u^{NN}) of forward wavefields $\underline{\mathbf{u}}^E$ and $\underline{\mathbf{u}}^N$ from sources in the east and north directions with weights to obtain the corresponding four rotated seismograms, \underline{u}^{TT} , \underline{u}^{TR} , \underline{u}^{RT} , and \underline{u}^{RR} , based on equation (5). Figure 2 shows that all the four rotated seismograms match very well with the corresponding reference seismograms, with numerical errors lower than 0.001%.

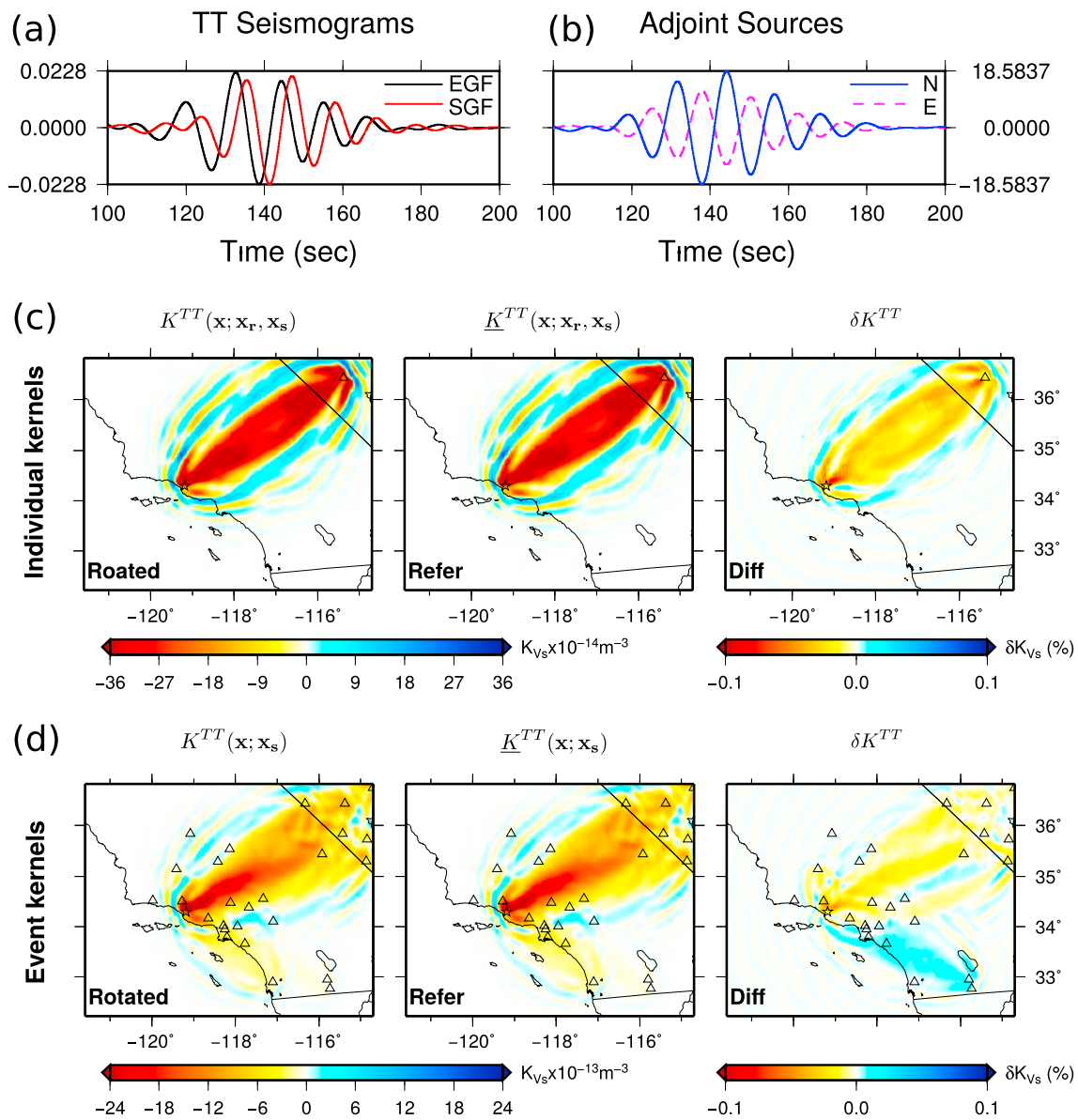


Figure 3. (a) T-T component seismograms of empirical Green's function (EGF; black line) and synthetic Green's function (SGF; red line) filtered between 10 and 20 s for the station pair CI.STC-TA.U11A. (b) The corresponding adjoint sources in the north (blue solid line) and east (magenta dash line) directions. Note the adjoint source in the vertical direction is set to zero. The adjoint sources are weighted by the sine/cosine ratio factors from equation (11), that is, $T = \cos \theta' E - \sin \theta' N$. (c) Rotated ($K^{TT}(\mathbf{x}; \mathbf{x}_r, \mathbf{x}_s)$, left), reference ($\underline{K}^{TT}(\mathbf{x}; \mathbf{x}_r, \mathbf{x}_s)$, middle) individual kernel, and their difference (δK^{TT} , right) for station pair CI.STC-TA.U11A at the depth of 15 km. The corresponding event kernels for all 26 stations are shown in (d). The kernel differences are shown in percentage relative to the maximum value of the reference kernels.

3.2. Individual Misfit Kernels

Using the reference seismogram \underline{u}^{TT} , we first construct the transverse-component adjoint source \underline{f}^{TT} to generate the adjoint field $(\underline{\mathbf{u}}^\dagger)^T$. The time convolution of the forward field $\underline{\mathbf{u}}^T$ and the corresponding adjoint field $(\underline{\mathbf{u}}^\dagger)^T$ results in the reference individual kernel $\underline{K}^{TT}(\mathbf{x}; \mathbf{x}_r, \mathbf{x}_s)$ (Figure 3c, middle). On the other hand, the rotated seismogram u^{TT} can also be used to compute the adjoint source f^{TT} (Figure 3a). With the proper amplitude modulation factors (equation (11)), this adjoint source is injected in the east and north directions (Figure 3b) at the receiver to construct the adjoint field, which is then convolved with the two forward fields \mathbf{u}^E and \mathbf{u}^N to generate two kernels in two separate adjoint simulations (Figure S2) as indicated by equation (16). The summation of these two kernels gives the final rotated individual kernel $K^{TT}(\mathbf{x}; \mathbf{x}_r, \mathbf{x}_s)$ for the T-T component EGF (Figure 3c, left). This summed kernel is almost the same as the reference individual kernel $\underline{K}^{TT}(\mathbf{x}; \mathbf{x}_r, \mathbf{x}_s)$ with their differences less than 0.1% (Figure 3c, right) at the depth of 15 km. Note

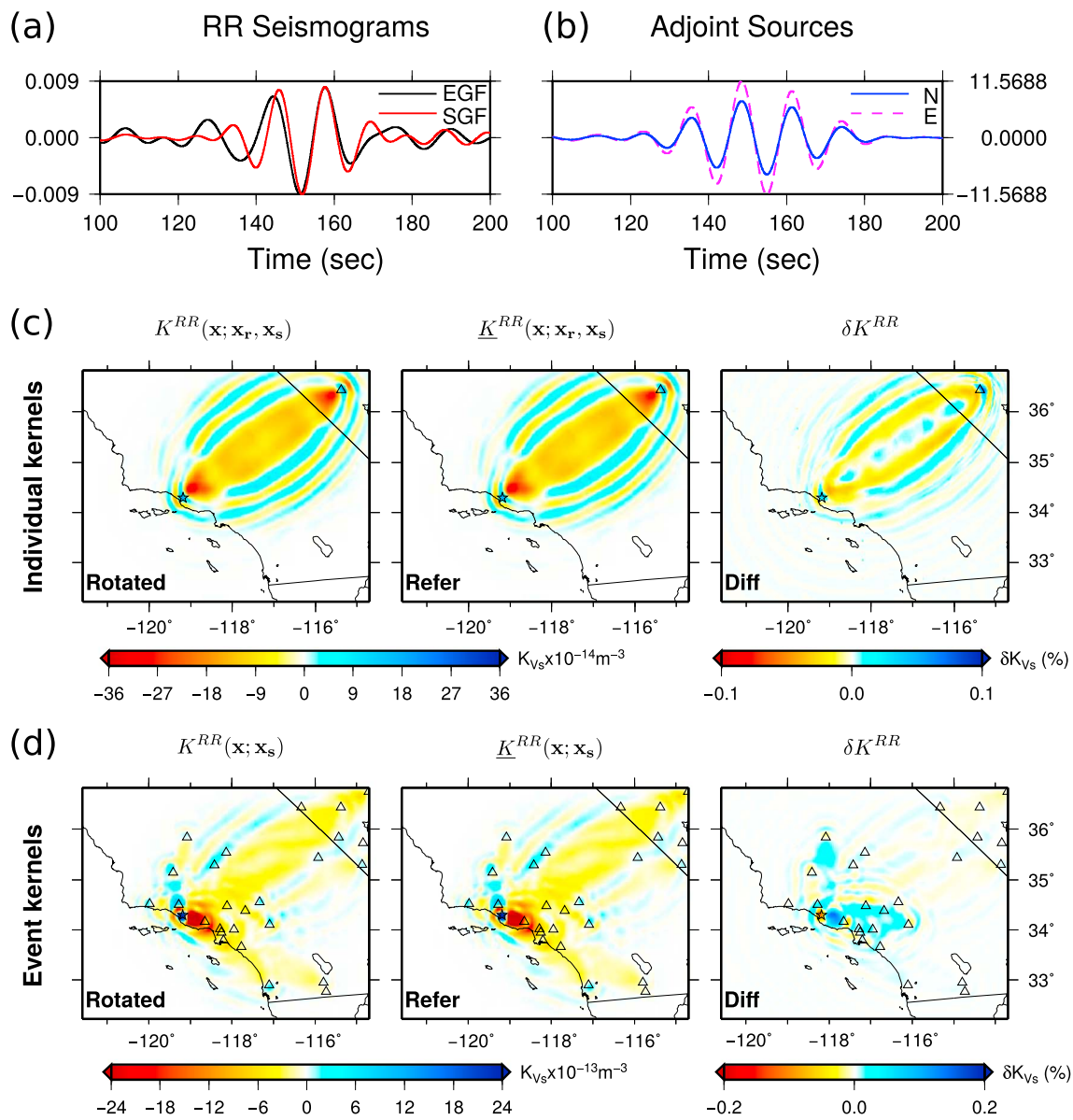


Figure 4. Similar to Figure 3 but for R-R component. The two adjoint sources in the east and north directions are weighted by $R = \sin \theta' E + \cos \theta' N$. EGF = synthetic Green's function; SGF = synthetic Green's function.

these adjoint sources are bandpass filtered between 10 and 20 s (same as in section 3.3). These errors are larger than those of the waveform shown in Figure 2b, which is most likely due to increasing errors of the SEM simulation with period as a result of imperfect absorbing boundary condition (Figure S3). Nevertheless, sensitivity kernels with less than 0.1% numerical errors are accurate enough for practical tomographic applications.

3.3. Event Misfit Kernels

For the T-T component EGF measurements at the 26 receivers in Figure 1c, the constructions of a reference and a rotated event kernel entail significantly different numbers of numerical simulations. The reference T-T component event misfit kernel $\underline{K}^{TT}(\mathbf{x}, \mathbf{x}_s)$ is computed by a summation of 26 reference individual misfit kernels, which is performed only for benchmarking purpose and is not practical in real applications of adjoint tomography given its high computational cost. In comparison, the rotated T-T component event misfit kernel $K^{TT}(\mathbf{x}, \mathbf{x}_s)$ is obtained by the summation of two event kernels, each of which is calculated by the convolution of a forward field from an east/north direction point-force source and an adjoint field from

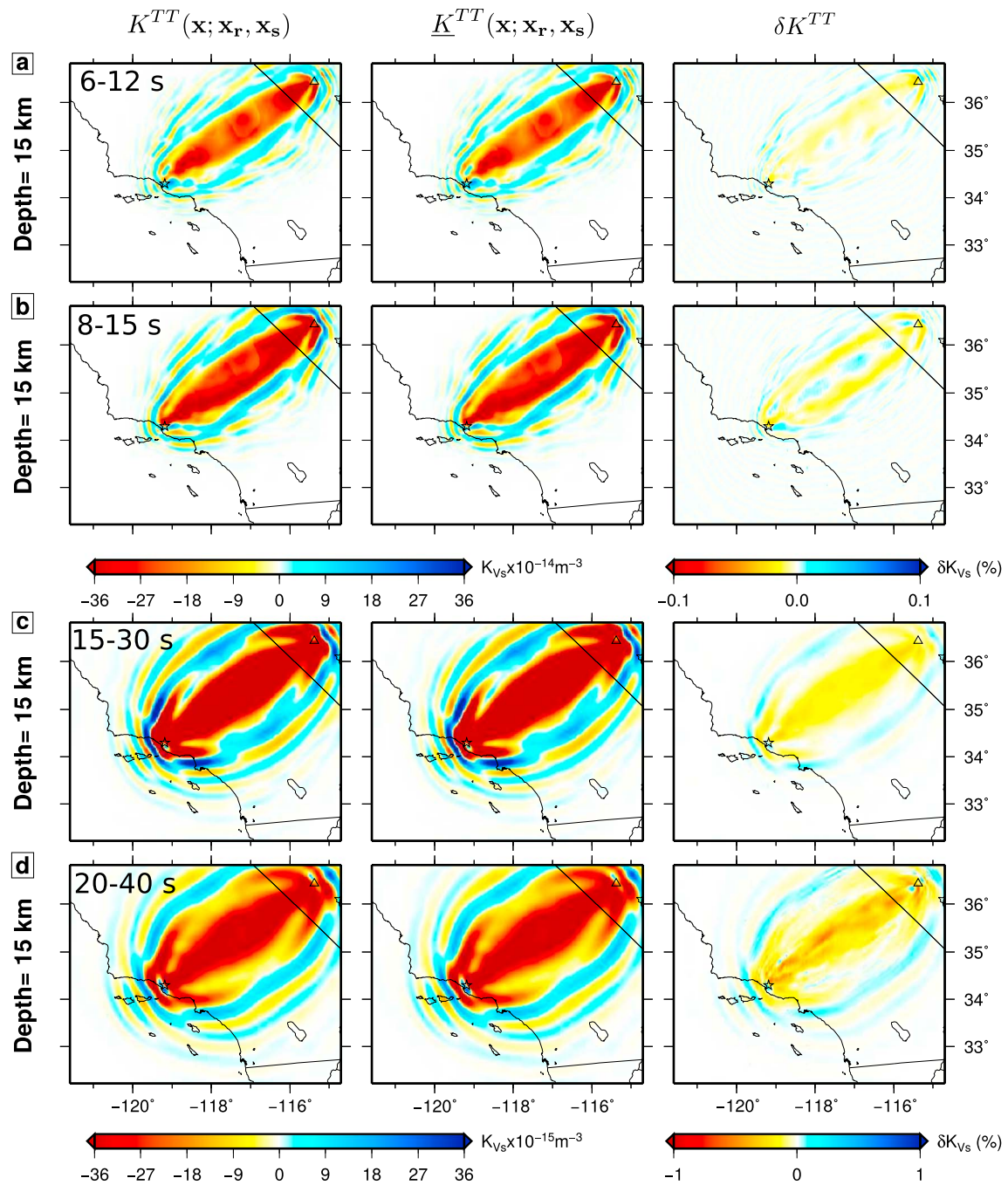


Figure 5. Rotated ($K^{TT}(\mathbf{x}; \mathbf{x}_r, \mathbf{x}_s)$), reference ($\underline{K}^{TT}(\mathbf{x}; \mathbf{x}_r, \mathbf{x}_s)$) individual kernel, and their difference (δK^{TT}) for station pair CI.STC-TA.U11A at the depth of 15 km in the four narrow period bands: 6–12, 8–15, 15–30, and 20–40 s.

properly constructed adjoint sources injected at all receivers simultaneously. Figure 3d shows the rotated T-T event kernel $K^{TT}(\mathbf{x}, \mathbf{x}_s)$ (left panel), the reference event kernel $\underline{K}^{TT}(\mathbf{x}, \mathbf{x}_s)$ (middle panel), and their differences (right panel) at the depth of 15 km. Similar to Figure 3c, the errors between the two kernels are less than 0.1%. The rotation relationships for R-R component individual and event kernels, given by equations (17) and (18), are also benchmarked against the references as demonstrated in Figure 4.

3.4. Sensitivity Kernels at Multiple Period Bands

We further validate the rotated kernels for T-T component at four other narrow period bands of 6–12, 8–15, 15–30, and 20–40 s, as shown in Figure 5. The errors of rotated kernels increase slightly with period but are

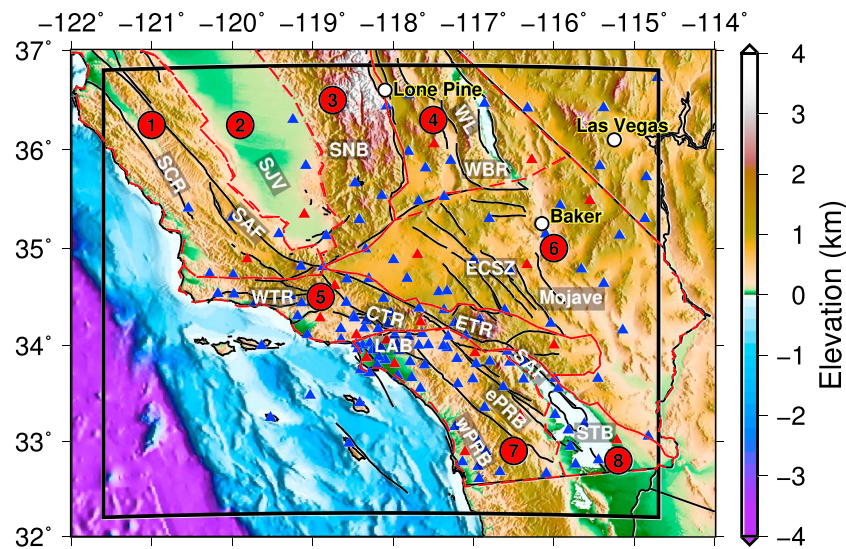


Figure 6. Map of southern California shown with topography, bathymetry and active faults (bold black lines). The 148 stations used in this tomographic study are shown as triangles out of which 19 selected for line search are shown in red. Labels 1–8 denote eight geomorphic provinces: (1) Coast Ranges, (2) Great Central Valley, (3) Sierra Nevada, (4) Basin and Range, (5) Transverse Ranges, (6) Mojave Desert, (7) Peninsular Ranges, and (8) Colorado Desert. Geological features labeled in bold white over transparent black boxes are indicated for reference: SCR = southern Coast Range; SAF = San Andreas Fault; SJV = San Joaquin Valley; SNB = Sierra Nevada Batholith; WL = Walker Lane; WBR = Western Basin and Ranges; WTR, CTR, and ETR = western, central, and eastern Transverse Ranges; ECSZ = Eastern California shear zone; LAB = Los Angeles Basin; ePRB and wPRB = east and west Peninsular Ranges Batholith; STB = Salton Trough Basin.

generally very small (less than 1%). The waveform differences between reference and rotated seismograms are shown in Figures S3 and S4. The adjoint sources at these five period bands are presented in Figures S5 and S6, and R-R component individual kernels at multiple period bands are plotted in Figure S7. In summary, these benchmarks demonstrate that the rotated seismograms, individual, and event misfit kernels computed based on equation (5), (15)–(18), and (19) are equivalent to the references with very small numerical errors.

4. Application to Imaging V_{SH} Structures of Southern California

To demonstrate the practicability of our kernel computation method for horizontal-component EGFs, we apply it to Love-wave adjoint tomography based on T-T component EGFs in southern California. In this section, we briefly introduce the data processing procedures to retrieve Love-wave signals from ambient noise, explain the inversion procedures, discuss the data misfit evolution in our adjoint tomography and present our V_{SH} model.

4.1. Data Processing Procedures

In our previous study (Wang et al., 2018), vertical-component ambient noise data are processed to obtain Z-Z component Rayleigh wave EGFs, which are utilized to iteratively improve the earthquake-based adjoint tomographic model **M16** of southern California (Tape et al., 2009, 2010). In this study, we extract T-T component NCFs from ambient seismic noise recorded at the 148 stations in southern California (Figure 6) from 2006 to 2012, by processing the north and east component seismograms simultaneously following the three-component noise data processing procedures described by Lin et al. (2008). In total, we obtain 10,869 T-T component NCFs with high-quality Love wave signals, which are then converted to EGFs by taking their negative time derivatives (Wang et al., 2018).

4.2. Inversion Procedures

The inversion procedures adopted here are similar to those of Rayleigh-wave ANAT, as elaborated in Wang et al. (2018). Here, we briefly summarize the inversion iteration procedure with a focus on the Love waves:

- (1) Forward simulations: For each master station, we conduct two forward simulations with point-force sources placed in the north and east directions, respectively. The resulting four seismograms (north-north

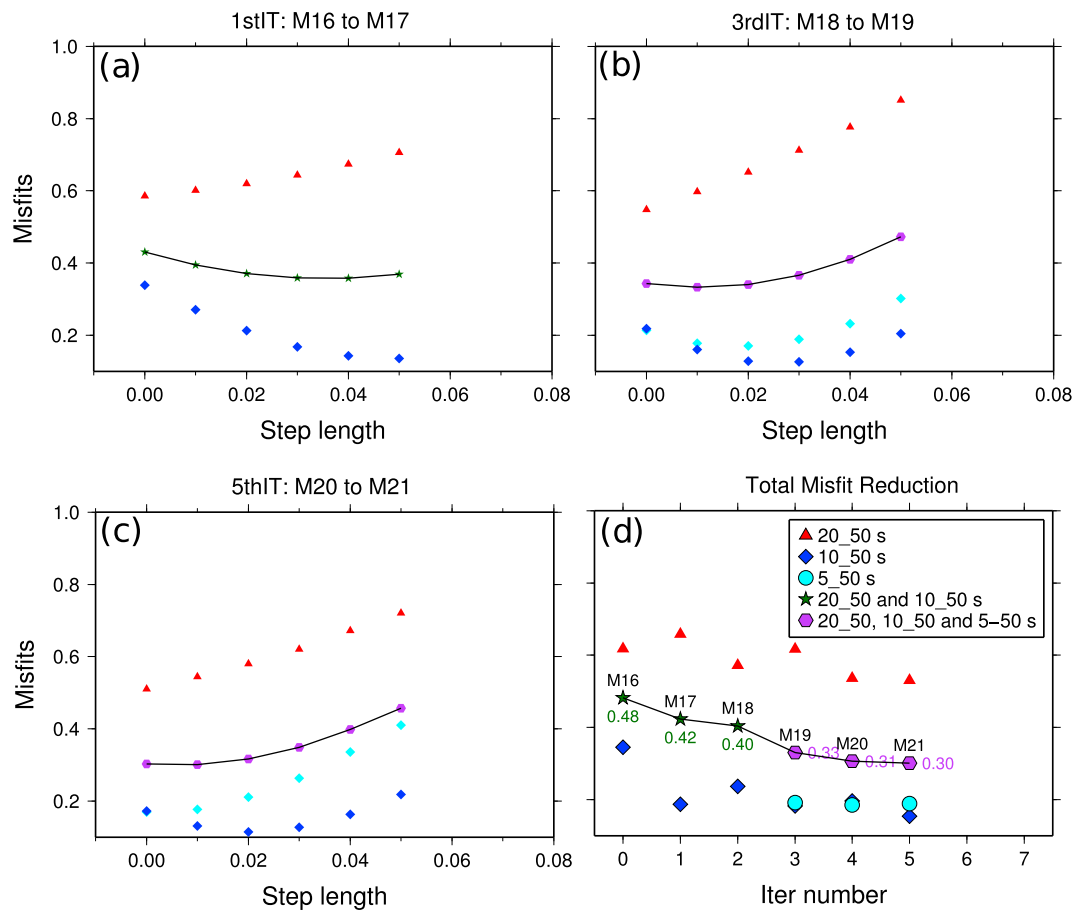


Figure 7. (a–c) Line search results at first (1stIT), third (3rdIT), and fifth (5thIT) iteration showing the variation of misfit function values as a function of step length for various period bands and the total misfit (also connected by solid curves); (d) total misfit reduction over five iterations. Note the total misfit is a dimensionless quantity that is the average value of individual traveltimes weighted by their uncertainties (down to 1 s; Wang et al., 2018) for all available period bands.

and north-east components from the source in the north, east-north, and east-east components from the source in the east) at receivers are rotated to obtain T-T component SGFs based on equation (9).

- (2) Preprocessing: For each EGF-SGF pair, we measure the frequency-dependent traveltimes and construct the adjoint sources at three period bands of 5–50, 10–50, and 20–50 s using a multitaper technique (Laske & Masters, 1996; Tape et al., 2010; Zhou et al., 2006). The adjoint sources of the three period bands at the receiver are added up to form the final adjoint source.
- (3) Adjoint simulation: The T-T component adjoint sources are rotated to the east and north directions and injected simultaneously at all receivers to generate the adjoint fields, which interact with the forward fields to obtain the two rotated event kernels, respectively.
- (4) Postprocessing: Rotated event kernels for all master stations are summed, preconditioned, and smoothed to obtain the final misfit gradient. The scale lengths of the Gaussian function used for smoothing are the same as those in the Rayleigh-wave ANAT study (Wang et al., 2018).
- (5) Line search: The optimal step length for the model update is determined based on the line search of a representative subset of 19 master stations (red triangles in Figure 6) distributed almost evenly throughout the study region, following the practice in many other adjoint tomography studies (e.g., Chen et al., 2014; Zhu et al., 2015).
- (6) Model update: A new model is obtained using the optimal step length. If the corresponding misfit reduction from last iteration is less than or equal to 3%, the iteration ends; otherwise, the next iteration starts by going back to step 1.

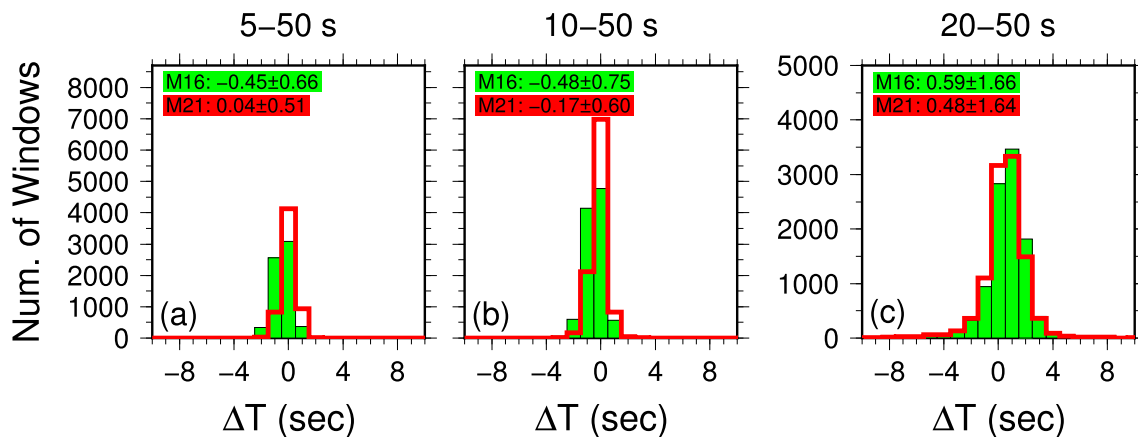


Figure 8. Traveltime misfit histograms obtained for model **M16** (green solid bars), **M21** (red bars) for the three period bands: (a) 5–50 s, (b) 10–50 s, and (c) 20–50 s. The horizontal axis denotes the cross-correlation time differences (ΔT) between data and synthetics, and the vertical axis indicates the number of windows for a given time shift range. The inset texts show the mean and standard deviation of all misfits in a certain period band for the two models.

Following the above procedures, we iteratively update the initial model **M16** using a multiscale strategy to improve data fitting. In the Rayleigh-wave type ANAT, we start our inversion with measurements made only from a long period band of 20–50 s and progressively add measurements at 10–50 and 5–50 period bands when the misfit reduction over iterations from existing band(s) becomes less evident. This strategy is effective and essential for the inversion to avoid being trapped in local minima when the initial model has relatively large misfits (average 2.1 s for 20- to 50-s band for Rayleigh waves). However, for Love waves in this study, as the misfits of our initial model are quite small (on average 0.59 s for 20- to 50-s band), to avoid overfitting the data, we decide to include the measurements of 10- to 50-s and 20- to 50-s period bands simultaneously in the first two iterations (from **M16** to **M18**) and then add the 5- to 50-s band in subsequent iterations. Figures 7a–7c show the line search and step length selection from the first, third, and fifth iteration. The evolution of the total misfit reduction over iterations plotted in Figure 7d shows that the total misfit decreases significantly in the first three iterations before it flattens out. After the fifth iteration, the total misfit shows very little change (reduction is 3%), and the inversion is terminated.

4.3. Inversion Results

We take **M21** from the fifth iteration as our final V_{SH} model. In this section, we discuss its improvement over the initial **M16** model by comparing the cross-correlation-based differential traveltimes measurements and briefly examine the main velocity features of the final model relative to **M16**.

4.3.1. Travelttime Misfits

Figure 8 shows the histograms of differential travelttime measurements made between EGFs and SGFs for both **M16** and **M21** model. For the initial model **M16**, most travelttime misfits at the three period bands are distributed within $[-2, +2]$ s, indicating that **M16**, built solely on earthquake data, produces good initial fits between SGFs and EGFs. However, the asymmetric distribution of the misfit histograms as well as the relatively large standard deviation (STD) suggests that there is room for improvement. For example, at 5- to 50-s and 10- to 50-s band, the misfit distributions are slightly biased toward the negative side, meaning the shallow structure of the model is on average faster than **M16**. On the contrary, at the 20- to 50-s band, the distribution is biased toward the positive side, suggesting the velocities are on average slower than **M16** at greater depths.

Further comparison between the histograms for **M16** and the final model **M21** shows that the most significant improvements are obtained for the 10- to 50-s and 5- to 50-s period bands, with the means and STDs of misfits changing from -0.45 ± 0.66 s to 0.04 ± 0.51 s for the 5- to 50-s band (Figure 8a) and from -0.48 ± 0.75 s to -0.17 ± 0.60 s for the 10- to 50-s band (Figure 8b). In the long period band of 20–50 s, the reduction is relatively small with the mean and STD changing from 0.59 ± 1.66 s to 0.48 ± 1.64 s (Figure 8c).

4.3.2. The V_{SH} Model

As Love waves (e.g., in T-T component EGFs) are primarily sensitive to V_{SH} structures, the final **M21** model is considered as a V_{SH} model. Figure 9 displays the absolute shear wave speed of **M16** (left column), **M21** (central column), and the differences between them (right column). The model is masked based on amplitudes

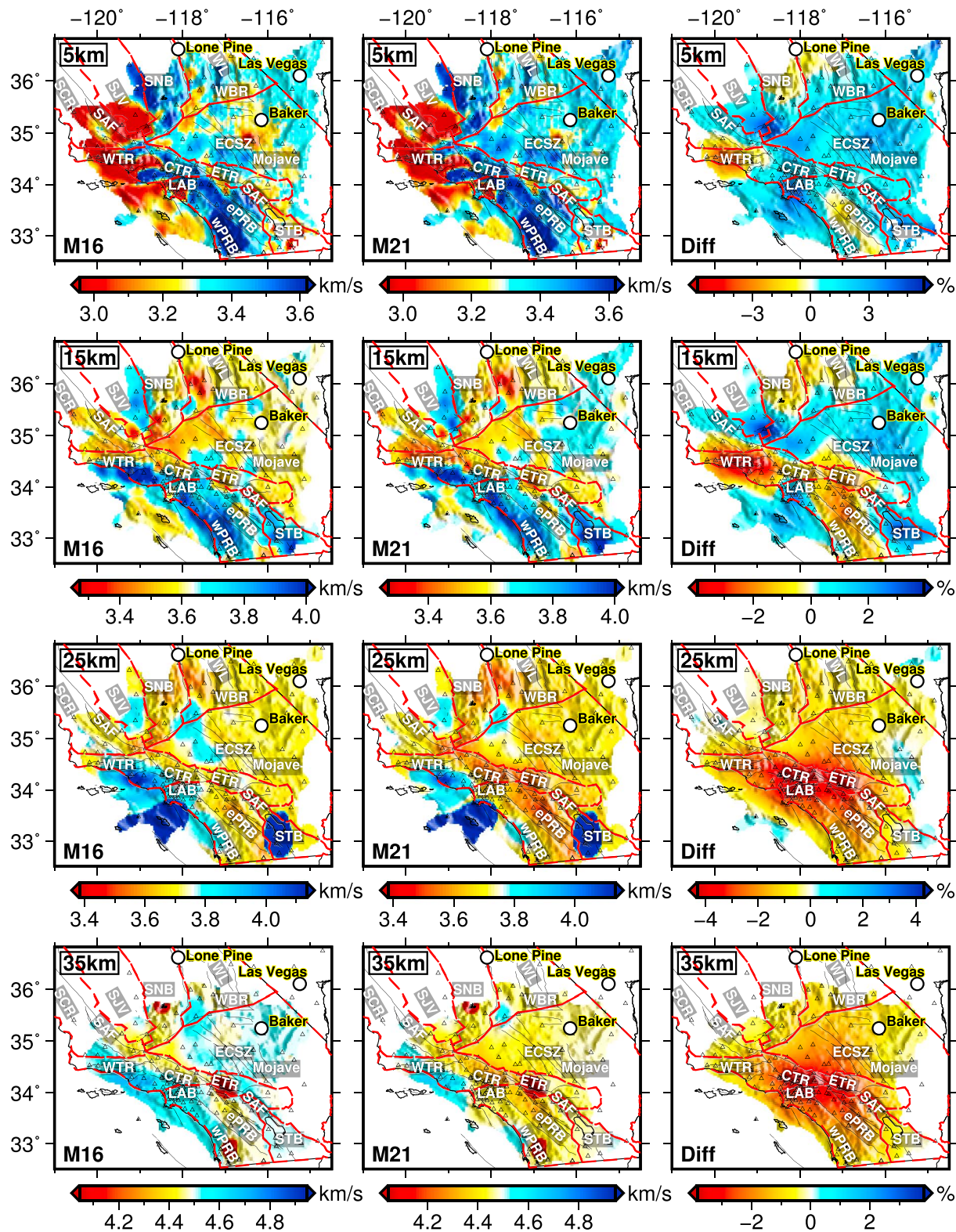


Figure 9. Horizontal slices of shear velocities for model **M16** (left panel), **M21** (middle panel), and their difference in percentage (right panel) at 5-, 15-, 25-, and 35-km depths.

of volumetric coverage kernels similar to that in Rayleigh-wave type ANAT (Wang et al., 2018). As inferred from the initial negative biases in the misfit distributions for 5- to 50-s and 10- to 50-s bands (Figures 8a and 8b), the V_{SH} in our model is generally enhanced at most parts of areas in the upper crust (5–15 km), including the southernmost edge of San Joaquin Valley and Sierra Nevada Batholith, most of the Mojave Desert, and the Salton Trough Basin, with changes reaching +6% at the southern area of San Joaquin Valley and Sierra Nevada Batholith at ~5-km depth. Absolute velocities at the Western Transverse Ranges, the Eastern Transverse Range, and the eastern Peninsular Ranges Batholith are slowed down by 4% in the middle crust (15 km). In the lower crust and uppermost mantle (≥ 25 km), V_{SH} generally becomes slower, which is particularly evident at the Central Transverse Ranges, Eastern Transverse Range, and Los Angeles Basin with changes reaching as much as -4%.

The above application demonstrates that it is feasible to carry out Love-wave ANAT and improve the waveform fitting of transverse-component EGFs using multicomponent sensitivity kernels computed based on our framework.

5. Discussions

In the above Love-wave ANAT, we note that the total misfit of Love waves (0.48) in the initial model, **M16**, is significantly smaller than that of Rayleigh waves (1.76; Wang et al., 2018) for the isotropic model, which suggests that the initial isotropic model fits the transverse-component surface waves better than those of the vertical and radial components, and the discrepancies between the final V_{SV} and V_{SH} models indicate the presence of radial anisotropy. In most traditional ambient noise tomographic studies on radial anisotropy, Z-Z and T-T component EGFs are usually combined to invert for V_{SV} and V_{SH} structures (e.g., Luo et al., 2013; Xie et al., 2013). Although we can combine the V_{SH} model from this study with the V_{SV} model from Wang et al. (2018) to generate a preliminary radially anisotropic model of southern California crust, we believe that it deserves a future study by simultaneously inverting both Rayleigh- and Love-wave EGFs with radially anisotropic kernels properly computed by the adjoint method. For anisotropic adjoint tomography of ambient noise, it is necessary to compute sensitivity kernels of the two horizontal components (K^{TT} and K^{RR}) as well as the vertical component (K^{ZZ}) for both V_{SV} and V_{SH} structures in a radially anisotropic model. This can be achieved by using the same rotation relationships (equations (5), (16), and (19)) except that the input 3-D Earth model for the forward and adjoint simulations becomes radially anisotropic. Furthermore, appropriate expressions should be used to represent V_{SV} and V_{SH} kernels for the generic operator in equation (1), as given by Sieminski et al. (2007) and Sales de Andrade and Liu (2017). In total, three forward and three adjoint simulations (to generate K^{ZZ} , K^{ET} , and K^{NT}) are required for anisotropic ANAT of both Z-Z and T-T component EGFs. If R-R component EGFs are also included in the inversion, two additional adjoint simulations (for K^{ER} and K^{NR}) are needed to obtain the R-R kernels.

In section 2, we show that only two forward and two adjoint simulations are required to calculate either individual or event kernels for T-T or R-R component EGF measurements. The derivations of multicomponent kernels can be readily extended to measurements on EGFs of cross-components (see Appendix B). For example, the kernel expression for the vertical-radial EGF is given by

$$\begin{aligned} K^{ZR}(\mathbf{x}; \mathbf{x}_r, \mathbf{x}_s) = & \mathbf{u}_z(\mathbf{x}, t; \mathbf{x}_s) \otimes [(\sin \theta' f^{ZR}) * \mathbf{u}_e(\mathbf{x}, T-t; \mathbf{x}_r) \\ & + (\cos \theta' f^{ZR}) * \mathbf{u}_n(\mathbf{x}, T-t; \mathbf{x}_r)]. \end{aligned} \quad (20)$$

Although we only show examples for traveltime misfit kernels, the expressions in section 2.2 are generic for other types of kernels as long as proper adjoint sources are used. For example, the sensitivity kernel of Rayleigh-wave ellipticity measured at a receiver is given by the difference between a radial and vertical-component amplitude kernel (e.g., $K_A^{ZZ} - K_A^{ZR}$), as demonstrated by Maupin (2017) and Bao and Shen (2018). Different from the plane waves used in Maupin (2017) and explosive sources used in Bao and Shen (2018), the use of point-force sources in our method might be more suitable for constructing 3-D Rayleigh wave ellipticity kernels for EGFs from ambient noise measurements. These 3-D Rayleigh wave ellipticity kernels can be used jointly with phase travelttime kernels for future adjoint tomography of ambient noise, providing better constraints on near-surface structures.

Throughout this study, we simply treat the negative time derivative of NCFs as EGFs and ignore the influence of unevenly distributed noise sources on the retrieval of EGFs (e.g., Basini et al., 2013; Ermert et al., 2017;

Stehly et al., 2006; Wang et al., 2014, 2016; Yang & Ritzwoller, 2008). It has been demonstrated that the uneven distribution of noise sources can introduce biases on the retrieved EGFs (e.g., Fichtner, 2014; Tsai, 2009), the extent of which has been estimated by a number of studies based on either analytic methods (e.g., Ermert et al., 2015; Froment et al., 2010; Xu et al., 2018; Yao & Van Der Hilst, 2009) or full wave numerical simulations (e.g., Fichtner, 2014; Tromp et al., 2010; Sager et al., 2017). Fichtner (2014) suggests that carrying out full waveform ANT without taking source heterogeneities and data processing schemes into account could introduce tomographic artifacts. On the other hand, Fichtner (2014) suggests that phase traveltimes measured at narrow bands are much less affected by source heterogeneities, which is corroborated by the similarities of phase velocity maps between earthquake-based tomography and ANT using phase traveltimes measurements (e.g., Shen et al., 2013; Yang et al., 2008; Yao et al., 2008). In the application of adjoint tomography to southern California presented in section 4, we build 3-D phase traveltimes misfit kernels based on the measurements using a multitaper technique (Laske & Masters, 1996; Tape et al., 2010; Zhou et al., 2004), which are weakly affected by source heterogeneities as demonstrated by Wang et al. (2018). Nevertheless, in the framework of full wave modeling, noise source effects can be accounted for by extending our method to ensemble forward and adjoint wavefields (Tromp et al., 2010) or transforming the actual sources and wave propagation physics into effective sources and wavefields (Fichtner et al., 2017; Sager et al., 2017), which is out of the scope of the current study and may be pursued in the future.

6. Conclusions

In this study, we develop a theoretical framework for calculating sensitivity kernels of multicomponent ambient noise EGFs for adjoint tomography. Our method is based on rotation relationships between wavefields generated by point-force sources acting in the north, east, and vertical directions, and their extension to calculate individual and event kernels. Our efficient multicomponent kernel computation method is validated for individual and event kernels in a 3-D isotropic Earth model based on full-wave numerical simulations and is demonstrated to be feasible for adjoint tomography in a study of V_{SH} structures of southern California crust. Furthermore, we show that our method can be extended to construct radially anisotropic and Rayleigh wave ellipticity kernels. Our method provides the basis for expanding ANAT from using only vertical-vertical component Rayleigh-wave EGFs to using all the multicomponent EGFs, and it paves the way for imaging radially anisotropic structures of the lithosphere by adjoint tomography based on both Rayleigh and Love waves from ambient noise.

Appendix A: Isotropic Sensitivity Kernels for Different Model Parameters

The expressions for density, shear, and bulk modulus (ρ , μ , κ) kernels of an isotropic model is given by (Liu & Tromp, 2006)

$$\begin{aligned} K_\rho &= -\rho(\mathbf{x}) \int_0^T [\partial_t^2 \mathbf{u}(\mathbf{x}, t; \mathbf{x}_s) \cdot \mathbf{u}^\dagger(\mathbf{x}, T-t; \mathbf{x}_r)] dt, \\ K_\mu &= -2\mu(\mathbf{x}) \int_0^T [\mathbf{D}(\mathbf{x}, t; \mathbf{x}_s) : \mathbf{D}^\dagger(\mathbf{x}, T-t; \mathbf{x}_r)] dt, \\ K_\kappa &= -\kappa(\mathbf{x}) \int [\nabla \cdot \mathbf{u}(\mathbf{x}, t; \mathbf{x}_s)] [\nabla \cdot \mathbf{u}^\dagger(\mathbf{x}, T-t; \mathbf{x}_r)] dt, \end{aligned} \quad (A1)$$

where \mathbf{D} and \mathbf{D}^\dagger denote the strain deviators for the forward and adjoint wavefield, respectively. Alternatively, we may choose the more commonly used model parameters as density, shear, and compressional wave speed (ρ' , β , α) given by

$$\begin{aligned} K_{\rho'} &= K_\rho + K_\mu + K_\kappa, \\ K_\alpha &= 2 \left(K_\mu - \frac{4}{3} \frac{\mu}{\kappa} K_\kappa \right), \\ K_\beta &= 2 \left(\frac{K_\kappa + \frac{4}{3} \mu}{\kappa} \right) K_\kappa. \end{aligned} \quad (A2)$$

Appendix B: Auxiliary Matrices for Cross-Component Ambient Noise EGFs

By utilizing the rotation matrix, equation (2), the auxiliary matrices in equation (6) related to the cross-component EGFs can be given as

$$\begin{aligned} C^{RT}(\theta, \theta') &= \begin{bmatrix} \sin \theta \cos \theta' & -\sin \theta \sin \theta' & 0 \\ \cos \theta \cos \theta' & -\cos \theta \sin \theta' & 0 \\ 0 & 0 & 0 \end{bmatrix}, C^{TR}(\theta, \theta') = \begin{bmatrix} \cos \theta \sin \theta' & \cos \theta \cos \theta' & 0 \\ -\sin \theta \sin \theta' & -\sin \theta \cos \theta' & 0 \\ 0 & 0 & 0 \end{bmatrix}, \\ C^{ZT}(\theta, \theta') &= \begin{bmatrix} 0 & 0 & 0 \\ 0 & 0 & 0 \\ \cos \theta' & -\sin \theta' & 0 \end{bmatrix}, C^{TZ}(\theta, \theta') = \begin{bmatrix} 0 & 0 & \cos \theta \\ 0 & 0 & -\sin \theta \\ 0 & 0 & 0 \end{bmatrix}, \\ C^{ZR}(\theta, \theta') &= \begin{bmatrix} 0 & 0 & 0 \\ 0 & 0 & 0 \\ \sin \theta' & \cos \theta' & 0 \end{bmatrix}, C^{RZ}(\theta, \theta') = \begin{bmatrix} 0 & 0 & \sin \theta \\ 0 & 0 & \cos \theta \\ 0 & 0 & 0 \end{bmatrix}. \end{aligned} \quad (B1)$$

Acknowledgments

The seismic data used in this study are downloaded from the Caltech/USGS Southern California Seismic Network (<https://doi.org/10.7914/SN/CI>) and IRIS Transportable Array (<https://doi.org/10.7914/SN/TA>). The authors would like to thank Editor Martha Savage, the associate editor, and two anonymous reviewers for their helpful suggestions, which significantly improved the manuscript. We also thank the developers of the software SPECFEM3D for their continued community work (<https://github.com/geodynamics/specfem3d>).

Computations for this study were performed on hardwares acquired through the combined funding of Canada Foundation for Innovation (CFI), Ontario Research Fund (ORF), and University of Toronto Startup Fund and partly hosted by the SciNet HPC Consortium. K. Wang is supported by the International Macquarie University Research Excellence Scholarship (iMQRES 43887678) and the Discovery Grants of the Natural Sciences and Engineering Research Council of Canada (NSERC) 487237. Y. Yang is supported by Australian Research Council Future Fellowship (FT130101220) and Discovery Project (DP190102940). This is contribution 1353 from the ARC Centre of Excellence for Core to Crust Fluid Systems (<http://www.cccf.mq.edu.au>) and 1316 in the GEMOC Key Centre (<http://www.gemoc.mq.edu.au>). Our final 3-D velocity model and codes are available from <https://sites.google.com/view/kaikaiwang/products>.

References

- Bao, X., & Shen, Y. (2018). Full-waveform sensitivity kernels of component-differential traveltimes and ZH amplitude ratios for velocity and density tomography. *Journal of Geophysical Research: Solid Earth*, 123, 4829–4840. <https://doi.org/10.1029/2017JB015421>
- Barmin, M., Ritzwoller, M., & Levshin, A. (2001). A fast and reliable method for surface wave tomography. *Pure and Applied Geophysics*, 158(8), 1351–1375. <https://doi.org/10.1007/PL00001225>
- Basini, P., Nissen-Meyer, T., Boschi, L., Casarotti, E., Verbeke, J., Schenk, O., & Giardini, D. (2013). The influence of nonuniform ambient noise on crustal tomography in Europe. *Geochemistry, Geophysics, Geosystems*, 14, 1471–1492. <https://doi.org/10.1002/ggge.20081>
- Bensen, G., Ritzwoller, M., Barmin, M., Levshin, A., Lin, F., Moschetti, M., et al. (2007). Processing seismic ambient noise data to obtain reliable broad-band surface wave dispersion measurements. *Geophysical Journal International*, 169(3), 1239–1260.
- Bensen, G., Ritzwoller, M., & Yang, Y. (2009). A 3-D shear velocity model of the crust and uppermost mantle beneath the United States from ambient seismic noise. *Geophysical Journal International*, 177(3), 1177–1196.
- Chen, M., Huang, H., Yao, H., Hilst, R., & Niu, F. (2014). Low wave speed zones in the crust beneath SE Tibet revealed by ambient noise adjoint tomography. *Geophysical Research Letters*, 41, 334–340. <https://doi.org/10.1002/2013GL058476>
- Ermert, L., Sager, K., Afanasiev, M., Boehm, C., & Fichtner, A. (2017). Ambient seismic source inversion in a heterogeneous earth: Theory and application to the Earth's hum. *Journal of Geophysical Research: Solid Earth*, 122, 9184–9207. <https://doi.org/10.1002/2017JB014738>
- Ermert, L., Villasenor, A., & Fichtner, A. (2015). Cross-correlation imaging of ambient noise sources. *Geophysical Journal International*, 204(1), 347–364.
- Fichtner, A. (2010). *Full seismic waveform modelling and inversion*. Verlag Berlin Heidelberg: Springer Science & Business Media.
- Fichtner, A. (2014). Source and processing effects on noise correlations. *Geophysical Journal International*, 197(3), 1527–1531.
- Fichtner, A., Stehly, L., Ermert, L., & Boehm, C. (2017). Generalised interferometry-I. Theory for inter-station correlations. *Geophysical Journal International*, 208(2), 603–638.
- Froment, B., Campillo, M., Roux, P., Gouédard, P., Verdel, A., & Weaver, R. L. (2010). Estimation of the effect of nonisotropically distributed energy on the apparent arrival time in correlations. *Geophysics*, 75(5), SA85–SA93.
- Gao, H., & Shen, Y. (2014). Upper mantle structure of the cascades from full-wave ambient noise tomography: Evidence for 3d mantle upwelling in the back-arc. *Earth and Planetary Science Letters*, 390, 222–233.
- Herrmann, R., & Ammon, C. (2004). Surface waves, receiver functions and crustal structure. Computer Programs in Seismology, Version 3.30. Saint Louis University.
- Laskie, G., & Masters, G. (1996). Constraints on global phase velocity maps from long-period polarization data. *Journal of Geophysical Research*, 101(B7), 16,059–16,075.
- Lee, E.-J., Chen, P., Jordan, T. H., Maechling, P. B., Denolle, M. A., & Beroza, G. C. (2014). Full-3-D tomography for crustal structure in southern California based on the scattering-integral and the adjoint-wavefield methods. *Journal of Geophysical Research: Solid Earth*, 119, 6421–6451. <https://doi.org/10.1002/2014JB011346>
- Lin, F.-C., Moschetti, M. P., & Ritzwoller, M. H. (2008). Surface wave tomography of the western United States from ambient seismic noise: Rayleigh and Love wave phase velocity maps. *Geophysical Journal International*, 173(1), 281–298.
- Lin, F.-C., Ritzwoller, M. H., Townend, J., Bannister, S., & Savage, M. K. (2007). Ambient noise rayleigh wave tomography of New Zealand. *Geophysical Journal International*, 170(2), 649–666.
- Liu, Q., & Gu, Y. (2012). Seismic imaging: From classical to adjoint tomography. *Tectonophysics*, 566, 31–66.
- Liu, Q., & Tromp, J. (2006). Finite-frequency kernels based on adjoint methods. *Bulletin of the Seismological Society of America*, 96(6), 2383–2397.
- Luo, Y. (2012). Seismic imaging and inversion based on spectral-element and adjoint methods (Ph.D. thesis), Princeton University.
- Luo, Y., Xu, Y., & Yang, Y. (2013). Crustal radial anisotropy beneath the Dabie orogenic belt from ambient noise tomography. *Geophysical Journal International*, 195(2), 1149–1164.
- Luo, Y., Yang, Y., Xu, Y., Xu, H., Zhao, K., & Wang, K. (2015). On the limitations of interstation distances in ambient noise tomography. *Geophysical Journal International*, 201(2), 652–661.
- Masters, G., Barmine, M., & Kientz, S. (2007). Mineos user's manual. Computational Infrastructure for Geodynamics.
- Maupin, V. (2017). 3-D sensitivity kernels of the Rayleigh wave ellipticity. *Geophysical Journal International*, 211(1), 107–119.
- Rawlinson, N., & Cambridge, M. (2004). Wave front evolution in strongly heterogeneous layered media using the fast marching method. *Geophysical Journal International*, 156(3), 631–647.
- Sabra, K. G., Gerstoft, P., Roux, P., Kuperman, W., & Fehler, M. C. (2005). Surface wave tomography from microseisms in Southern California. *Geophysical Research Letters*, 32, L14311. <https://doi.org/10.1029/2005GL023155>

- Sager, K., Ermert, L., Boehm, C., & Fichtner, A. (2017). Towards full waveform ambient noise inversion. *Geophysical Journal International*, 212(1), 566–590.
- Sales de Andrade, E., & Liu, Q. (2017). Fast computation of global sensitivity kernel database based on spectral-element simulations. *Pure and Applied Geophysics*, 174(7), 2733–2761.
- Shapiro, N. M., Campillo, M., Stehly, L., & Ritzwoller, M. H. (2005). High-resolution surface-wave tomography from ambient seismic noise. *Science*, 307(5715), 1615–1618.
- Shen, W., Ritzwoller, M. H., & Schulte-Pelkum, V. (2013). A 3-D model of the crust and uppermost mantle beneath the Central and Western US by joint inversion of receiver functions and surface wave dispersion. *Journal of Geophysical Research: Solid Earth*, 118, 262–276. <https://doi.org/10.1029/2012JB009602>
- Sieminski, A., Liu, Q., Trampert, J., & Tromp, J. (2007). Finite-frequency sensitivity of surface waves to anisotropy based upon adjoint methods. *Geophysical Journal International*, 168(3), 1153–1174.
- Stehly, L., Campillo, M., & Shapiro, N. (2006). A study of the seismic noise from its long-range correlation properties. *Journal of Geophysical Research*, 111, B10306. <https://doi.org/10.1029/2005JB004237>
- Tape, C., Liu, Q., Maggi, A., & Tromp, J. (2009). Adjoint tomography of the southern California crust. *Science*, 325(5943), 988–992.
- Tape, C., Liu, Q., Maggi, A., & Tromp, J. (2010). Seismic tomography of the southern California crust based on spectral-element and adjoint methods. *Geophysical Journal International*, 180(1), 433–462.
- Tape, C., Liu, Q., & Tromp, J. (2007). Finite-frequency tomography using adjoint methods—Methodology and examples using membrane surface waves. *Geophysical Journal International*, 168(3), 1105–1129.
- Tromp, J., Luo, Y., Hanasoge, S., & Peter, D. (2010). Noise cross-correlation sensitivity kernels. *Geophysical Journal International*, 183(2), 791–819.
- Tromp, J., Tape, C., & Liu, Q. (2005). Seismic tomography, adjoint methods, time reversal and banana-doughnut kernels. *Geophysical Journal International*, 160(1), 195–216.
- Tsai, V. C. (2009). On establishing the accuracy of noise tomography travel-time measurements in a realistic medium. *Geophysical Journal International*, 178(3), 1555–1564.
- Wang, K., Luo, Y., & Li, H. (2014). The nature of ambient noise over a field in western Junggar basin near Karamay, China, *The 6th International Conference on Environmental and Engineering Geophysics* (pp. 92–97). Xi'an, China: Xian.
- Wang, K., Luo, Y., & Yang, Y. (2016). Correction of phase velocity bias caused by strong directional noise sources in high-frequency ambient noise tomography: a case study in Karamay, China. *Geophysical Journal International*, 205(2), 715–727.
- Wang, K., Yang, Y., Basini, P., Tong, P., Tape, C., & Liu, Q. (2018). Refined crustal and uppermost mantle structure of southern California by ambient noise adjoint tomography. *Geophysical Journal International*, 215(2), 844–863. <https://doi.org/10.1093/gji/ggy312>
- Xie, J., Ritzwoller, M. H., Shen, W., Yang, Y., Zheng, Y., & Zhou, L. (2013). Crustal radial anisotropy across eastern Tibet and the western Yangtze craton. *Journal of Geophysical Research: Solid Earth*, 118, 4226–4252. <https://doi.org/10.1002/jgrb.50296>
- Xu, Z., Mikesell, T. D., & Gribler, G. (2018). Source-distribution estimation from direct Rayleigh waves in multicomponent crosscorrelations, *SEG Technical Program Expanded Abstracts 2018* (pp. 3090–3094). USA: Society of Exploration Geophysicists.
- Yang, Y., & Ritzwoller, M. H. (2008). Characteristics of ambient seismic noise as a source for surface wave tomography. *Geochemistry, Geophysics, Geosystems*, 9, Q02008. <https://doi.org/10.1029/2007GC001814>
- Yang, Y., Ritzwoller, M. H., Levshin, A. L., & Shapiro, N. M. (2007). Ambient noise Rayleigh wave tomography across Europe. *Geophysical Journal International*, 168(1), 259–274.
- Yang, Y., Ritzwoller, M. H., Lin, F.-C., Moschetti, M., & Shapiro, N. M. (2008). Structure of the crust and uppermost mantle beneath the western United States revealed by ambient noise and earthquake tomography. *Journal of Geophysical Research*, 113, B12310. <https://doi.org/10.1029/2008JB005833>
- Yao, H., Beghein, C., & Van Der Hilst, R. D. (2008). Surface wave array tomography in SE Tibet from ambient seismic noise and two-station analysis-II. Crustal and upper-mantle structure. *Geophysical Journal International*, 173(1), 205–219.
- Yao, H., & Van Der Hilst, R. D. (2009). Analysis of ambient noise energy distribution and phase velocity bias in ambient noise tomography, with application to SE Tibet. *Geophysical Journal International*, 179(2), 1113–1132.
- Yao, H., van Der Hilst, R. D., & Maarten, V. (2006). Surface-wave array tomography in SE Tibet from ambient seismic noise and two-station analysis-I. Phase velocity maps. *Geophysical Journal International*, 166(2), 732–744.
- Zhao, L., Jordan, T. H., Olsen, K. B., & Chen, P. (2005). Fréchet kernels for imaging regional earth structure based on three-dimensional reference models. *Bulletin of the Seismological Society of America*, 95(6), 2066–2080.
- Zhou, Y., Dahlen, F., & Nolet, G. (2004). Three-dimensional sensitivity kernels for surface wave observables. *Geophysical Journal International*, 158(1), 142–168.
- Zhou, Y., Nolet, G., Dahlen, F., & Laske, G. (2006). Global upper-mantle structure from finite-frequency surface-wave tomography. *Journal of Geophysical Research*, 111, B04304. <https://doi.org/10.1029/2005jb003677>
- Zhu, H. (2018). Crustal wave speed structure of North Texas and Oklahoma based on ambient noise cross-correlation functions and adjoint tomography. *Geophysical Journal International*, 214(1), 716–730.
- Zhu, H., Bozdog, E., Peter, D., & Tromp, J. (2012). Structure of the European upper mantle revealed by adjoint tomography. *Nature Geoscience*, 5(7), 493–498.
- Zhu, H., Bozdog, E., & Tromp, J. (2015). Seismic structure of the European upper mantle based on adjoint tomography. *Geophysical Journal International*, 201(1), 18–52.